

## EFFECT OF PROCESS PARAMETER VARIATION ON MICROSTRUCTURE AND MECHANICAL PROPERTIES OF ADDITIVELY MANUFACTURED Ti-6Al-4V

Jonathan Pegues<sup>1</sup>, Kelvin Leung<sup>2</sup>, Azadeh Keshtgar<sup>2</sup>, Luca Airoidi<sup>2</sup>, Nicole Apetre<sup>2</sup>;  
Nagaraja Iyyer<sup>2</sup>, Nima Shamsaei<sup>1,\*</sup>

<sup>1</sup>*Laboratory for Fatigue & Additive Manufacturing Excellence, Department of Mechanical Engineering, Auburn University, Auburn, AL 36849*

<sup>2</sup>*Technical Data Analysis, Inc., 3190 Fairview Park Dr., Suite 650, Falls Church, VA 22042*

\*Corresponding author: [shamsaei@auburn.edu](mailto:shamsaei@auburn.edu)

### **Abstract**

As additively manufactured (AM) parts become viable options for various structural applications, it is essential to fully understand how various process parameters affect their subsequent mechanical behavior. In this study, a process simulation package is utilized to model the heat transfer during the laser-based powder bed fusion (L-PBF) process. Along with mechanical properties, the model is capable of estimating porosity, density, and microstructural evolution during the rapid cooling phases associated with L-PBF. Simulation results were validated using experimentally measured mechanical properties of L-PBF Ti-6Al-4V specimens. Tensile tests and microscopy were conducted for determining the effects of process parameters (i.e. laser power, laser scan speed, hatch distance) on microstructure, strength, and ductility of fabricated parts. Predictions from process simulations were compared with experimental results. Validated process simulation packages, used and developed herein, can provide a low-cost means for the quality control of AM parts.

**Keywords:** Mechanical properties; Microstructure; Additive manufacturing; ICME; Titanium alloys

### **Introduction**

Recently additive manufacturing (AM) has gained much interest to be implemented in many structural applications across a wide variety of industries including biomedical and aerospace applications. It has been well established, however, that parts produced via AM are not comparable to their wrought counterparts showing varying strength and ductility with the later showing large reductions in the AM parts [1–4]. The differences in strength and ductility of AM parts when compared to their wrought counterparts is mostly attributed to the unique microstructural characteristics of the AM parts including grain structure, chemical composition, residual stresses, presence of micro-voids, lack of fusion, etc. On the other hand, tailoring purpose

specific materials through manipulation of process parameters to achieve a more desirable microstructure and mechanical properties is an intriguing aspect of the AM method [5]. Research has shown that many of these microstructural characteristics can be manipulated by adjusting the AM process parameters [6].

Experimentally determining the optimal process parameters for a desired microstructural or mechanical property requires a significant time investment coupled with high experimentation costs. In order to reduce these time and experimental costs a Process Parameter Optimizer (PPO) tool was developed to optimize the more critical process parameters. The framework utilizes a sensitivity analysis method to determine the process parameters which are most capable of altering the microstructure and resulting mechanical properties. The proposed PPO tool consists of an additive manufacturing (AM) simulation module, a sensitivity analysis of process parameters, and an AM process optimization module which are accompanied by supporting experiments to validate the simulation model. The PPO tool is ultimately designed to receive desired microstructural or mechanical properties by providing an optimized set of parameters through simulation.

### **Multi-scale AM Simulation Module**

A multi-layer multi-track L-PBF process of Ti-6Al-4V was simulated via a finite element (FE) model for the 3D heat transfer analysis and is shown in Figure 1. The heating of the powder layer is modeled using a time dependent heat transfer process which is similar to a diffusion process and given in Equation 1 where  $Q$ ,  $T$ ,  $C_p$ ,  $\rho$ , and  $k$  are the body heat source, the temperature, the specific heat, the density and the thermal conductivity of the material, respectively.

$$\rho C_p \frac{dT}{dt} = k \nabla^2 T + Q(x, t) \quad (1)$$

A representative section (3 mm × 5 mm × 0.5 mm) of the AM part was simulated with each deposited layer having the dimensions of 1 mm × 5 mm × 0.1 mm. The convergence of the maximum temperature was predicted through two models with different mesh refinement at the center of the top surface. To achieve convergence, the average element size was set to approximately the laser beam radius. A Goldak double ellipsoid volumetric heat source profile [7] was used to model the laser input to the sample. Additionally, a subroutine developed by Technical Data Analysis, Inc. (TDA) was implemented to model the motion of the laser scan path.

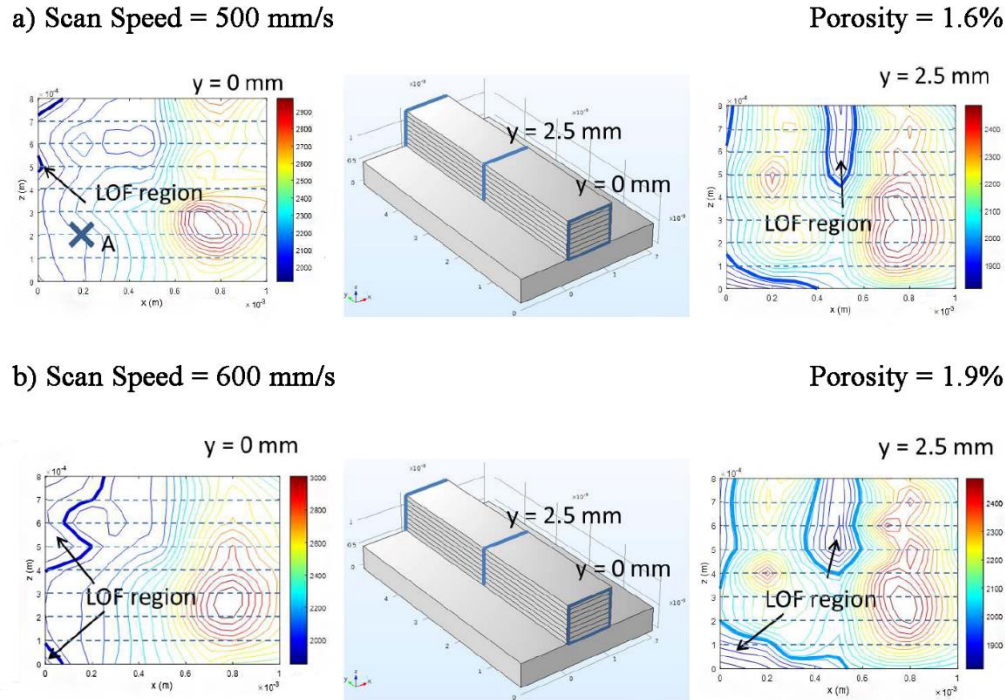


Figure 1: Simulation results for lack of fusion zones for scan velocities of a) 0.5 m/s and b) 0.6 m/s.

One of the most influential microstructural characteristics for AM parts is the lack of fusion between subsequent layers. These void-like areas have very little volume and therefore do not result in a significant loss of density, however, their flat geometry results in greater stress concentrations than typical spherical voids. Model simulations were conducted with the specific intent of modeling the lack of fusion zones within an AM part. Six AM process input parameters were selected to study their effects on final temperature and porosity, and include laser beam power ( $P$ ), efficiency of the laser beam ( $\eta$ ), laser beam radius ( $c$ ), laser scan speed ( $v$ ), ambient temperature ( $T_{amb}$ ), and absorptivity of the material ( $\alpha$ ). To illustrate the heat transfer simulation, the temperature history of two selected controlled points in the simulation domain for  $v = 5 \text{ mm/s}$  at different locations of the domain are presented in Figure 1. Figure 1 also shows the maximum temperature achieved during the simulation at two cross section locations. The lack of fusion (LoF) regions can be determined by the maximum temperature plots. Incomplete melting occurs when the maximum temperature achieved during the simulation is less than the melting temperature of Ti-6Al-4V. For convenience, the LoF regions are depicted in the figures by thicker contour lines. By sampling sections, the porosity of the AM part can be estimated by summing up the volume of the LoF regions. Results from the simulation show an increase in lack of fusion areas with increasing scan speed as shown in Figure 1.

## Sensitivity Analysis

The AM process can be affected by a multitude of build parameters; however, the effect of each parameter may be insignificant when compared to others. To reduce computational and experimental time costs, a sensitivity analysis was conducted to determine which parameters will show the greatest effects on the AM parts.

TDA has developed a novel global sensitivity analysis method based on Sobol's index and Latin Hypercube Sampling (LHS). The proposed global sensitivity analysis approach varies all variables simultaneously through its entire range by LHS while considering the interaction between different parameters (such as laser power and beam width). The LHS method has the ability to recreate the input distribution through sampling in fewer iterations when compared with the Monte Carlo method. Fewer iterations for LHS is achieved by stratification of the input probability distributions. Sobol's method uses the decomposition of variance to calculate the Sobol's sensitivity indexes [8]. Sobol's approach decomposes the function  $f(x)$  into summands of increasing dimensionality, as shown in Equation 2.

$$f(x_1, \dots, x_k) = f_0 + \sum_{i=1} f_i(x_i) + \sum_{1 \leq i < j \leq k} f_{ij}(x_i, x_j) + \dots + f_{1,2,\dots,k}(x_1, \dots, x_k) \quad (2)$$

The mean and variance of the parameters are calculated using Equation 3 and Equation 4 where  $N$  is the sampling size and  $x_{-i} = (x_1, \dots, x_{i-1}, x_{i+1}, \dots, x_m)$  is the parameter combination complementary to  $x_i$ :

$$f_0 = \int f(x) dx \approx \frac{1}{N} \sum_{k=1}^N f(x_k) \quad (3)$$

$$D = \int f^2(x) dx - f_0^2 \approx \frac{1}{N} \sum_{k=1}^N f^2(x_k) - f_0^2 \quad (4)$$

The partial variance or first order effects are computed for each parameter by fixing the values of that parameter and varying the remaining parameters. Both primary and complementary parameter spaces are needed to implement Equation 5.

$$D_i = D - \frac{1}{2} \int [f(x) - f(x_i, x'_{-i})]^2 dx dx'_{-i} \approx D - \frac{1}{2N} \sum_{k=1}^N [f(x_k) - f(x_{ik}, x'_{-ik})]^2 \quad (5)$$

The total sensitivity effects are computed for all the chosen parameters using Equation 6.

$$D_i^{tot} = \frac{1}{2} \int [f(x) - f(x_i, x'_{-i})]^2 dx dx'_{-i} \approx \frac{1}{2N} \sum_{k=1}^N [f(x_k) - f(x'_{ik}, x_{-ik})]^2 \quad (6)$$

The parameters are then sorted according to their sensitivities.

A Matlab code developed by TDA was used to implement the described approach to Sobol's index. Three process parameters were selected as a focus on the global sensitivity analysis. These parameters include laser power, laser scan velocity, and laser beam width. A Monte Carlo Simulation was implemented for the simulation model with the process parameter ranges given in Table 1. A total of 100 iterations were conducted for the select ranges with the maximum temperature being estimated via the heat transfer module previously mention and recorded for each iteration. Figure 2 shows the calculated results of the first order effects as well as the total effects for each parameter. From these results, it can be seen that the laser scan velocity was the most sensitive for the ranges given while the laser beam width showed the least sensitivity. It should be noted, however, that there is an intrinsic relationship between the laser power and laser beam width, however, compared to laser power the effect of scan velocity is much higher (Fig. 2). It should be mentioned here that these specific results are limited to the TDA simulation data and the specified process parameters listed in Table 1. These results are not necessarily applicable directly to other case studies. It is recommended to implement a complete proposed global sensitivity analysis for each case study individually.

Table 1: Process parameter values used for sensitivity analysis.

L-PBF Parameter	Mean Value	Lower Bound	Upper Bound
Laser Power (W)	280	252	308
Laser Scan Velocity (m/s)	1.20	1.08	1.32
Laser Beam Spot Size (m)	5.0e-5	4.5e-5	5.5e-5

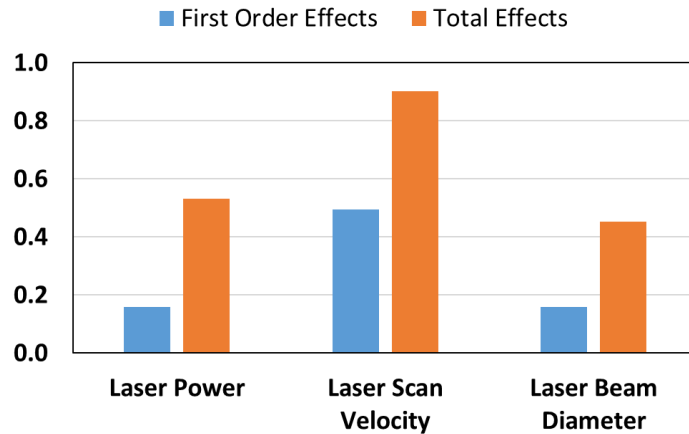


Figure 2: First order and total effects for the given process parameters.

## Experimental Results

### Specimen Design and Fabrication

In order to validate the model simulations, a series of tensile tests were conducted on a set of AM fabricated samples with varying process parameters. A total of three process parameters were chosen to experimentally determine the effect each had on the mechanical properties of the AM parts. The process parameters chosen for this research was laser power, scan velocity, and hatch spacing. The process parameters can be separated into three categories in which two of the three parameters are held constant to produce a set of varying laser power, scan velocities, and hatch spacing as shown in Table 2. The general set of parameters for Ti-6Al-4V provided with the AM machine is given as parameter set two, which is bolded in Table 2 and included as a base for each of the three categories.

*Table 2: Parameter sets used to produce the AM parts separated into their respective categories.*

Parameter	Laser Power (W)	Scan Speed (mm/s)	Hatch Distance ( $\mu\text{m}$ )
1	252	1200	140
<b>2</b>	<b>280</b>	<b>1200</b>	<b>140</b>
3	308	1200	140
10	336	1200	140
11	364	1200	140
14	280	840	140
13	280	960	140
4	280	1080	140
2	280	1200	140
5	280	1320	140
7	280	1200	126
2	280	1200	140
6	280	1200	154
16	280	1200	168

Specimens were fabricated using a powder bed based EOS M290 with a maximum laser power of 400W. The spherical Ti-6Al-4V alloy powder was supplied with a powder size greater than 15  $\mu\text{m}$  and less than 45  $\mu\text{m}$ . Specimens were built horizontally onto a titanium substrate as shown in Figure 3 with the given dimensions. Three to four samples were produced for each parameter set given in Table 2. The specimens were stress relieved before removal from the plate to remove any residual stress as result of the increased cooling rates associated with the L-PBF process. The stress relief was conducted at 700° C for 1 hr under an Ar environment and allowed to air cool. Upon removal, each specimen surface was lightly ground by hand in order to make more accurate cross-sectional measurements of the cross-section.

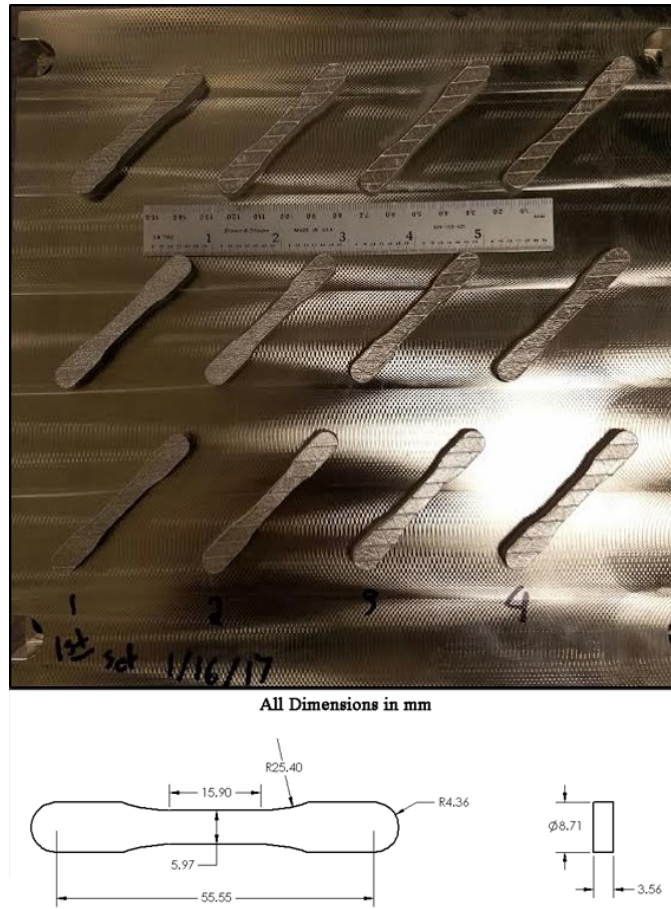


Figure 3: Sample orientation on build plate and specimen dimensions.

Tensile tests were conducted on a servo-hydraulic MTS testing frame with a load capacity of 100 kN. The tests were conducted in strain control with a strain rate of 0.001  $\text{s}^{-1}$  until sufficiently past the yield stress ( $\sigma_y$ ) after which the test was continued in displacement control until final fracture. Fracture surfaces were removed along with a portion of the gage section for further

microstructural analysis. The fracture surfaces were observed using a scanning electron microscope with an excitation voltage of 20 kV. The as-built and removed gage sections were prepared using standard metallographic procedures. The microstructure was revealed using a mixture of 92 ml of distilled water, 6 ml of nitric acid, and 2 ml of hydrofluoric acid with each sample being immersed for 20 – 30 s. The microstructure consisted of mostly alpha ( $\alpha$ ) and martensite ( $\alpha'$ ) grains within elongated prior beta ( $\beta$ ) grains. The  $\alpha'$  grains are readily observable by the acicular grains within the prior  $\beta$  grains as shown in Figure 4. The prior  $\beta$  grains show equiaxed grains parallel to the build direction (Fig. 4(a)) while showing more elongated grains perpendicular to the build direction due to epitaxial grain growth (Fig. 4(b)).

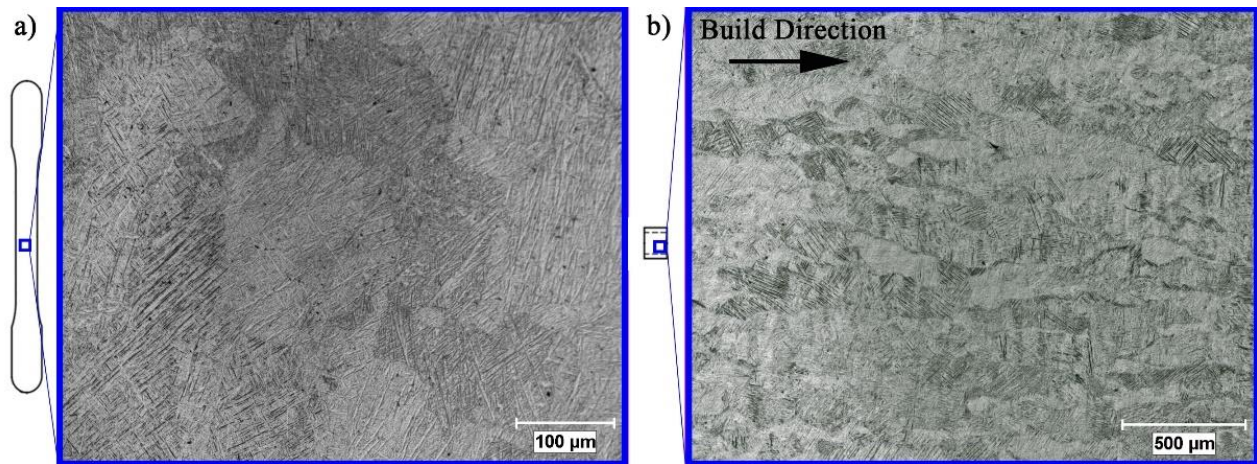


Figure 4: Microstructure of AM parts for a) longitudinal direction and b) cross section direction.

### **Tensile Behavior**

The tensile properties were mostly similar across all process parameters with the only exception being elongation to failure and fracture strain as shown in Table 3. AM parts produced by L-PBF typically show increases in yield stress ( $\sigma_y$ ) ultimate tensile strength (UTS) with decreasing ductility when compared to their wrought counterparts which was observed for the present investigation and shown in Table 3.

Table 3: Tensile properties for each parameter set.

Parameter	E	$\sigma_y$	UTS	Elong.	$\sigma_f$	$\epsilon_f$
#	GPa	MPa	MPa	%	MPa	%
1	95.8	1084	1133	3.40	1170	3.28
<b>2</b>	<b>102.0</b>	<b>1079</b>	<b>1130</b>	<b>2.83</b>	<b>1168</b>	<b>3.31</b>
3	102.4	1111	1169	3.88	1213	3.78
4	99.0	1063	1112	3.81	1153	3.65
5	98.0	1071	1127	4.04	1158	3.65
6	97.6	1074	1136	4.60	1183	4.35
7	99.5	1066	1133	5.35	1186	4.98
10	95.8	1050	1123	3.04	1156	2.95
11	99.4	1068	1137	4.24	1183	4.07
13	100.3	1052	1118	4.27	1165	4.08
14	97.3	1073	1136	5.65	1189	5.35
16	94.9	1073	1144	4.72	1185	4.23
Wrought (average)	113.0	880	950	14.00	/	/

### Computed Tomography Scan

X-ray tomography was conducted on a Shimadzu Safire Medical Tomosynthesis system. Three scans of middle regions of 3 coupons were performed and are shown in Figure 5. The tomography results show that, the most consistent production defects of these specimens are: (a) surface roughness, (b) voids, and (c) inclusions. The tomography results showed a much greater number of voids in sample #5 as shown in Figure 5. Along with this significantly greater number of voids present within the specimens compared to the other tested samples, was a much rougher surface, 33.42  $\mu\text{m}$  compared to 24.55 (Sample # 3) and 16.94 (Sample #6). Interestingly, sample

set # 5 had a greater scan speed (1.32 m/s) compared to sample #3 and #6 (1.20 m/s). As previously mentioned, the scan velocity showed the higher sensitivity and the simulation showed that increasing scan velocity would result in higher lack of fusion (void) area.

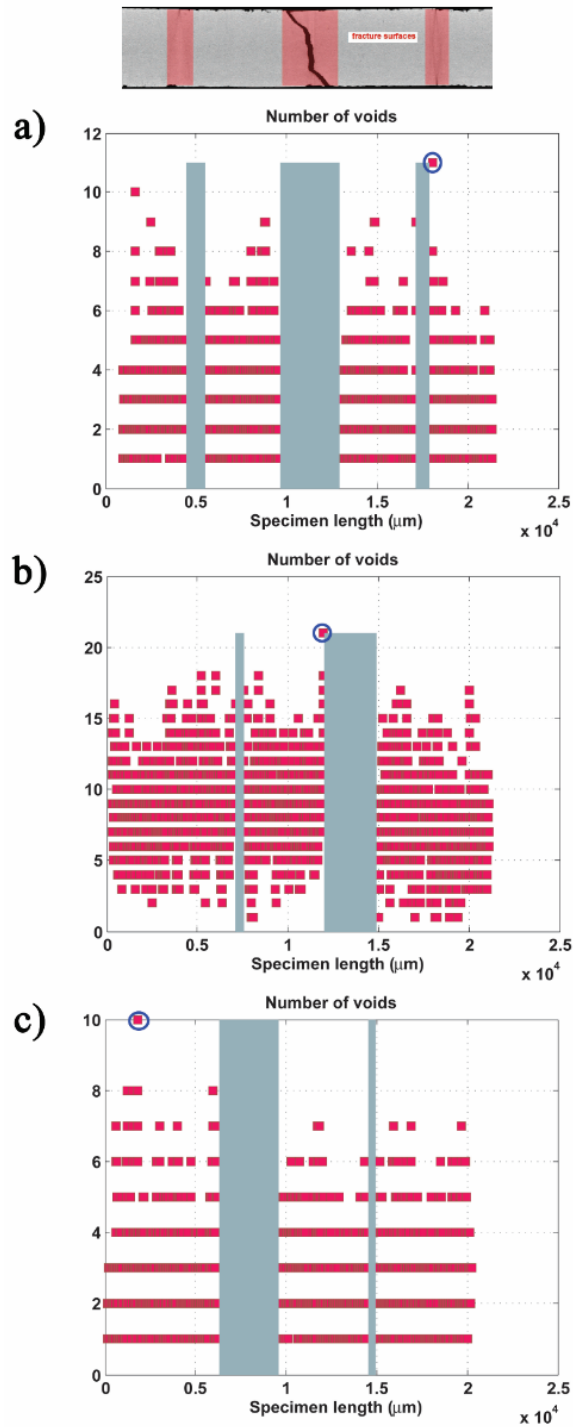


Figure 5: Tomography results for three selected specimens.

## Fractography

The fracture surfaces of selected samples were observed with a scanning electron microscope (SEM). Two characteristic surfaces were readily observable for all fractured specimens, a fibrous area and a ductile overload area. The fibrous area is shown in Figure 6 outlined in red and is characterized by transgranular quasi-cleavage fracture. The ductile overload area, shown outside the fibrous area, shows shear failure characteristics. In the fibrous zone a combination of ductile fracture and cleavage fracture is observed. Striations consistent with fracture along the  $\alpha'$  phase are observable in the fibrous section of the fracture surfaces as shown in Figure 6 (blue). The ductile overload area shows a more elongated dimpled structure with the characteristic shear angle approximately  $45^\circ$  from the fibrous section as shown in Figure 6 (red).

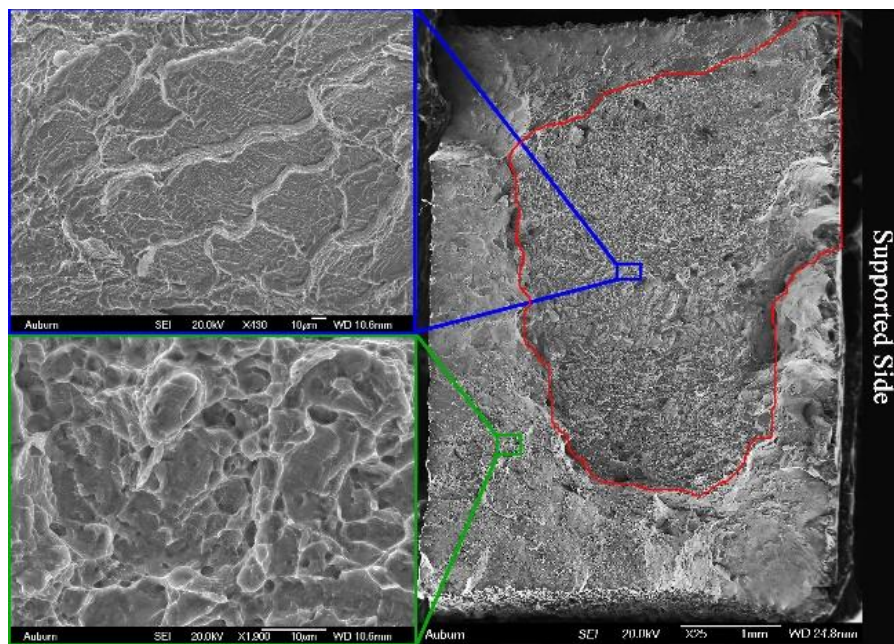


Figure 6: Fracture surface of selected tensile sample showing the fibrous area outlined in red.

## Discussion

Ti-6Al-4V with an  $\alpha'$  microstructure shows much less ductility than its  $\alpha + \beta$  counterparts [9] and behaves in a more similar manner to cast Ti-6Al-4V. As such, the L-PBF produced Ti-6Al-4V parts with high  $\alpha'$  phase fractions would be expected to show much lower ductility than their wrought counterparts. However, the high  $\alpha'$  microstructure does not explain the variation in ductility between the parameter sets observed in this investigation. Additive manufactured parts can be more susceptible to quasi-brittle fracture due to the type of defects intrinsic to the L-PBF process such as the lack of fusion between layers and voids throughout the parts. These defects can also result in lower ductility for AM parts when compared to their wrought counterparts. These effects can be readily observed when comparing the fracture toughness of the three specimens used

for tomography. Comparing just the tomography samples, it can be seen that the sample with the highest number of voids (sample #5) had the lowest ductility while the sample with the lowest number of voids (sample #6) had the highest ductility.

The sensitivity analysis discussed previously predicted that scan velocity would have the most effect on the maximum temperature during the building process and therefore could show the most effect on the mechanical properties. The experimental validation was able to demonstrate this effect as shown in Figure 7 where, compared to laser power and hatch distance, changes in scan velocity showed much greater effects on the ductility. Increasing scan velocity results in a decrease in true fracture strain resulting in less ductility. The decrease in ductility is most likely a result of a higher fraction of  $\alpha'$  phase due to more rapid heating and cooling along the beam path for higher scan velocities. Research has shown that wrought Ti-6Al-4V alloys with high  $\alpha'$  phase fractions show much less ductility compared to their  $\alpha + \beta$  counterparts [9]. As such, additively manufactured Ti-6Al-4V parts by L-PBF with intrinsically high cooling rates resulting in higher  $\alpha'$  should show similar behavior. Continuing this logic, L-PBF produced parts with lower scan velocities should show a lower fraction of the  $\alpha'$  phase with an improvement in ductility compared to higher scan velocities.

Laser power showed some effect on ductility, however, not as consistently or to the same effect as scan velocity. Generally, higher laser power resulted in greater ductility, however, it can be seen in Figure 7(b) that the second highest laser power resulted in the lowest ductility. Hatch distance showed relatively no effect on the ductility of the AM parts. The lack of effect of hatch size on ductility is not surprising since it does not affect the volumetric energy associated with the interaction of the beam and powder. There should be some slight effect on the cooling rate for a given point on the build, however, compared to the effect of scan velocity and laser power, hatch distance would not be expected to show large variations in temperature.

## Conclusions

In summary, a multi-scale AM simulation module developed by TDA was implemented to simulate the effect of varying process parameters on the AM produced parts. A sensitivity analysis was then conducted to determine which of the process parameters in the AM process could affect the mechanical properties of the AM parts the most. It was predicted that the AM parts would show more sensitivity to scan velocity than laser power. Simulation showed that increasing scan velocities would result in greater porosity and lack of fusion areas. Tomography analysis of the AM produced parts showed that the sample with the highest scan velocity contained a much higher number of voided areas than lower scan velocities. Further experimental analysis then showed that the ductility of the AM parts was more sensitive to scan velocity compared to laser power validating the sensitivity analysis. Additionally, changes in the process parameters showed little effect on  $\sigma_y$  and UTS while showing more effect on the ductility of the AM parts.

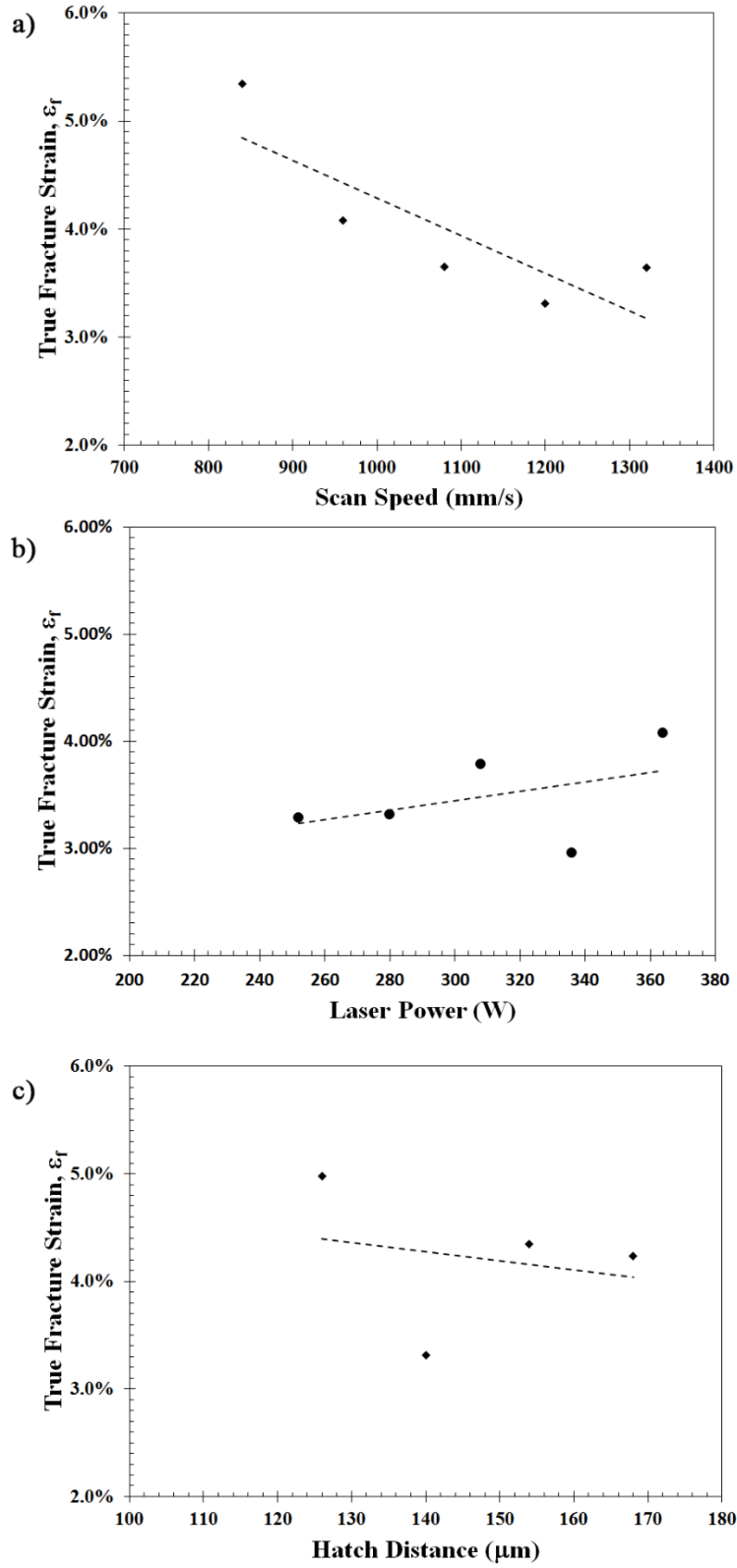


Figure 7: Process parameter effects on true fracture strain.

## Acknowledgements

The funding from the Naval Air Systems Command (NAVAIR) is greatly appreciated. The authors would like to also thank Professor Andrew Makeev for the tomography results which were carried out at the Advanced Materials and Structures Lab (AMSL) at University of Texas at Arlington.

## References

- [1] N. Shamsaei, A. Yadollahi, L. Bian, and S. M. Thompson, “An overview of Direct Laser Deposition for additive manufacturing; Part II: Mechanical behavior, process parameter optimization and control,” *Addit. Manuf.*, vol. 8, pp. 12–35, Oct. 2015.
- [2] A. J. Sterling, B. Torries, N. Shamsaei, S. M. Thompson, and D. W. Seely, “Fatigue behavior and failure mechanisms of direct laser deposited Ti–6Al–4V,” *Mater. Sci. Eng. A*, vol. 655, pp. 100–112, Feb. 2016.
- [3] E. Brandl, F. Palm, V. Michailov, B. Viehweger, and C. Leyens, “Mechanical properties of additive manufactured titanium (Ti–6Al–4V) blocks deposited by a solid-state laser and wire,” *Mater. Des.*, vol. 32, no. 10, pp. 4665–4675, Dec. 2011.
- [4] L. E. Murr *et al.*, “Microstructures and mechanical properties of electron beam-rapid manufactured Ti–6Al–4V biomedical prototypes compared to wrought Ti–6Al–4V,” *Mater. Charact.*, vol. 60, no. 2, pp. 96–105, Feb. 2009.
- [5] A. B. Spierings, G. Levy, and K. Wegener, “Designing material properties locally with additive manufacturing technology SLM,” 2014.
- [6] H. Gong, K. Rafi, H. Gu, T. Starr, and B. Stucker, “Analysis of defect generation in Ti–6Al–4V parts made using powder bed fusion additive manufacturing processes,” *Addit. Manuf.*, vol. 1, pp. 87–98, Oct. 2014.
- [7] J. Goldak, A. Chakravarti, and M. Bibby, “A new finite element model for welding heat sources,” *Metall. Trans. B*, vol. 15, no. 2, pp. 299–305, Jun. 1984.
- [8] I. M. Sobol, “Sensitivity analysis for nonlinear mathematical models,” *Math. Model. Comput. Exp.*, vol. 1, pp. 407–414, 1993.
- [9] H. Matsumoto *et al.*, “Room-temperature ductility of Ti–6Al–4V alloy with  $\alpha'$  martensite microstructure,” *Mater. Sci. Eng. A*, vol. 528, no. 3, pp. 1512–1520, Jan. 2011.